Original Research

Imaging and Pathologic Evaluation of Cryoablation of Woodchuck (*Marmota monax*) Hepatocellular Carcinoma

Juan A Esparza-Trujillo,[1] William F Pritchard,[1] Michal Mauda-Havakuk,[1] Matthew F Starost,[2] Paul Wakim,[4] Johnathan Zeng,[1] Andrew S Mikhail,[1] Ivane Bakhutashvili,[1] Bradford J Wood,[1,3] and John W Karanian[1,*]

We characterized cryoablation as a mode of clinical intervention in adult woodchucks with hepatocellular carcinoma (HCC). Woodchucks (*n* = 4) were infected with woodchuck hepatitis virus at birth and developed LI-RADS-5 hypervascular HCC. At 21 mo of age, they underwent ultrasound (US), contrast-enhanced CT (CECT) imaging, and US-guided subtotal cryoablation (IcePearl 2.1 CX, Galil, BTG) of their largest tumor (Mean HCC volume of 49 ± 9 cm^3). Cryoablation was performed using two 10-min freeze cycles, each followed by an 8-min thaw cycle. The first woodchuck developed significant hemorrhage after the procedure and was euthanized. In the other 3 woodchucks, the probe track was cauterized and all 3 completed the study. Fourteen days after ablation, CECT was performed, and woodchucks were euthanized. Explanted tumors were sectioned using subject-specific, 3D-printed cutting molds. Initial tumor volume, the size of the cryoablation ice ball, gross pathology and hematoxylin and eosin–stained tissue sections were evaluated. On US, the edges of the solid ice balls were echogenic with dense acoustic shadowing and average dimensions of $3.1 \pm 0.5 \times 2.1 \pm 0.4$ cm and cross-sectional area of 4.7 ± 1.0 cm^2. On day 14 after cryoablation, CECT of the 3 woodchucks showed devascularized hypo-attenuating cryolesions with dimensions of $2.8 \pm 0.3 \times 2.6 \pm 0.4 \times 2.93 \pm 0.7$ cm and a cross-sectional area of 5.8 ± 1.2 cm^2. Histopathologic evaluation showed hemorrhagic necrosis with a central amorphous region of coagulative necrosis surrounded by a rim of karyorrhectic debris. A rim of approximately 2.5 mm of coagulative necrosis and fibrous connective tissue clearly demarcated the cryolesion from adjacent HCC. Partial cryoablation of tumors produced coagulative necrosis with well-defined ablation margins at 14 d. Cauterization appeared to prevent hemorrhage after cryoablation of hypervascular tumors. Our findings indicate that woodchucks with HCC may provide a predictive preclinical model for investigating ablative modalities and developing new combination therapies.

Abbreviations and acronyms: CECT, contrast-enhanced CT; HCC, hepatocellular carcinoma; US, ultrasound

Introduction

Hepatocellular carcinoma (HCC) is the sixth most prevalent neoplasm and the fourth most frequent cause of cancer-related mortality globally.[10] For many patients, heat-based therapies such as radiofrequency and microwave ablation are viable treatment options.[12] Cryoablation also appears to be safe and as effective as heat-based methods of ablation in certain situations.[5,12,27,28] Cryoablation kills tumor tissue by freezing, forming an ice ball, by using the expansion of compressed argon in the cryoprobe to generate probe temperatures as low as −140 °C (−220 °F), resulting in formation of an ice ball and subsequent tumor necrosis.[6,7,13] Intraprocedural imaging of the ice ball and postprocedural imaging of the ablation zone may confirm technical success including the adequacy of ablated zone of the targeted tumor.[26]

Evaluation of HCC therapies may benefit from a preclinical model that recapitulates the natural course of the disease in humans. Eastern woodchucks (*Marmota monax*) infected chronically with woodchuck hepatitis virus spontaneously develop HCC that is similar in size, vascularity, and heterogeneity to human HCC,[9,19,20,24,29] making this a useful model for evaluation of therapies intended for treatment of hepatitis-induced tumors in humans.[1,8,14] However, few studies have evaluated the use of woodchuck HCC as a model for image-guided device-based interventional procedures such as heat and cold-based ablative therapies.[2,3,22,25,30] The current study determined the feasibility of performing cryoablation in woodchucks with HCC and evaluated imaging and correlative pathology after subtotal cryoablation.

Materials and Methods

Animals. Four woodchucks with HCC (3 female, mean weight 3.1 kg; 1 male, weight 3.0 kg; mean age, 21 mo) were acquired from Northeastern Wildlife (Harrison, ID). The vendor had inoculated the woodchucks with woodchuck hepatitis virus within their first week of life and confirmed them as tumor positive based on serum γ-glutamyl transpeptidase levels

greater than 50 IU/L and ultrasound (US) prior to our procurement.[15] Woodchucks were housed individually with ad libitum access to food (NIH 23GD Rabbit Diet, 5L7Z, Test Diet, Richmond, IN) and water and provided with fresh produce twice daily. Animals were housed in modified stainless steel cages (28 × 28 × 34.5 in. [71.1 × 71.1 × 87.6 cm]) with shredded aspen bedding (Nepco, Warrensburg, NY) provisioned with a wooden gnawing block (BioServ, Flemington, NJ) and a stovepipe nest box. Room conditions were maintained with temperature between 72 ± 2 °F (22.2 ± 1 °C), relative humidity of less than 70%, and a 12:12-h light:dark cycle (lights on, 0600). All animals were observed and monitored at least once daily by trained facility staff. The study was conducted under an animal use protocol (DRD16-03) approved by the IACUC at the National Institutes of Health in an AALAC-accredited animal facility in compliance with U.S. Animal Welfare Regulations.

Animal procedures. All woodchucks underwent US and contrast-enhanced CT (CECT) to identify HCC tumors and plan treatment. The woodchucks were sedated with 5% isoflurane delivered via an induction chamber, followed by a mixture of preanesthetic agents (28.6 mg/kg ketamine HCl and 5 mg/kg xylazine, IM), and were then maintained on 1% to 5% isoflurane and 100% oxygen (2 L/min) delivered via a rabbit mask for the duration of the procedure. Woodchucks were shaved and prepared for surgery using aseptic technique while under anesthesia.

An abdominal US examination was performed (Philips iU22, Philips, Bothell, WA), followed by venipuncture of the cephalic vein with a 21- or 23-gauge angiocatheter for multidetector CT imaging (Brilliance MX8000 IDT 16-section detector CT; Philips, Andover, MA). After noncontrast CT of the chest and liver, multiphase imaging of the liver was performed with bolus tracking and power injection (MEDRAD Stellant CT Injection System; Bayer Healthcare, Leverkusen, Germany) of 3.0 mL of iopamidol (Isovue-370; Bracco Diagnostics, Monroe Township, NJ) followed by 3.0 mL of 0.9% saline solution, all at 0.2 mL/s. Multiphasic imaging was acquired in the early arterial (4-s delay), late arterial (23-s delay), portal venous (43-s delay), and late parenchymal (63-s) phases. Scans were obtained at 120 kVp and a tube current of 225 mA with a 180-cm field of view and image reconstruction of 0.8-mm sections at 0.4-mm intervals. The target tumor was the largest tumor identified in each subject and was categorized by a clinical radiologist under the Liver Imaging-Reporting and Data System (LI-RADS)[20] and tumor volume was determined.

Cryoablation. Subtotal cryoablation of HCC tumors (*n* = 4) was performed using a 14-gauge cryoprobe (IcePearl 2.1 CX 90°, Boston Scientific, Marlborough, MA) under US guidance. The treatment algorithm was two, 10-min freeze cycles, each followed by an 8-min passive thaw cycle. US imaging was performed during ablation, including imaging at the conclusion of the final freeze cycle. The edge of the ice ball was identified by the echogenic rim, which was created by the acoustic impedance mismatch between the solid ice ball and the adjacent tissue; acoustic shadowing beyond the rim was due to the loss of US signal.

The first woodchuck was euthanized after probe removal due to hemorrhage. The probe track of the other 3 animals was cauterized during probe withdrawal. After probe removal, external pressure was applied over the liver puncture site for 2 to 3 min and noncontrast CT of the liver was acquired. The 3 woodchucks then recovered from anesthesia and were maintained for 14 days. Postprocedural recovery was uneventful; daily health checks and observations including biweekly

physical exams by veterinary staff showed normal behavior and food consumption.

Imaging and tissue collection after cryoablation. Tissue cutting molds were designed and 3D printed based on each subject's CT scan from the time of cryoablation. The mold was oriented so that the cutting planes were parallel to the axis of the probe track at 5 mm intervals. This placement allowed direct comparison of multiplanar reformatted radiologic images to gross and histologic evaluation of the liver.[21] On day 14 after cryoablation, the woodchucks were placed under general anesthesia and both noncontrast and multiphasic contrast enhanced CT of the liver were performed as before. The woodchucks were euthanized by exsanguination under deep anesthesia and confirmatory administration of a combination of pentobarbital sodium, 390 mg/mL, and phenytoin sodium, 50 mg/mL (Euthasol 1 mL/10 lb.; Virbac Animal Health, Fort Worth, TX). Hepatic and tumor tissue were excised, placed in the subject-specific molds, and 5-mm-thick slices were cut. Tissue slices were grossly examined and fixed in 10% formalin. Histologic sections were stained with hematoxylin and eosin (H and E). Histopathologic analysis was performed by a board-certified veterinary pathologist.

Imaging and tissue analysis. The long axis and the half-width of the orthogonal short axis of the ice ball were measured on an US that was acquired at the conclusion of the second freeze cycle in an imaging plane that included the cryoprobe. The short axis length of the ice ball was reported as twice the measured half-width. Cross-sectional area was calculated as an ellipsoid. The ablation zone at 14 d was measured using multiplanar reformatted CT images to generate a plane that included the long axis trajectory of the probe for measurement of the ellipsoidal cross-sectional area as with the US image. An orthogonal plane was defined, the short axes of the ablation zone were measured in 2 dimensions (OsiriX 10.0.5 Pixmeo, Geneva, Switzerland), and tumor volume was calculated as an ellipsoid, $(4/3)\pi \cdot x \cdot y \cdot z$, where x, y, and z are the dimensions of the tumor. Reconstruction of the target tumor and 14-d ablation zone CTs were performed using Mimics Research (version 20.0; Materialise, Leuven, Belgium) to generate a 3D volumetric rendering. Dimensions of the ablation zone were measured on the histologic section that included the probe track, and cross-sectional area was calculated.

Statistical analysis. A paired *t* test was performed to compare cross sectional area measurements between the intraprocedural ice ball on US and the 14-d ablation zone on CT and histopathology (*n* = 3). A Pearson correlation and linear regression analysis of cross-sectional area was also performed. All data are expressed as mean ± SE.

Results

Preprocedural imaging. US and CT imaging revealed large tumors in all 4 woodchucks. The tumors were hypervascular with hyperenhancement in the early or late arterial phases as compared with the appearance of liver without tumor. A board-certified pathologist categorized the target tumors as LIRADS-5.[20] HCC tumors had a mean volume of 49 ± 9 cm³ and an ellipsoidal shape (Figure 1).

Cryoablation. Cryoablation of the target tumor was successfully performed under US guidance in all woodchucks (Figure 2) with recovery of 3 of 4 subjects. The first subject developed significant intra-abdominal hemorrhage when the probe was withdrawn after cryoablation, and this woodchuck was therefore euthanized. To prevent hemorrhage in the remaining 3 woodchucks, the probe track was cauterized using the cautery function during slow withdrawal of the cryoprobe at a rate of

Figure 1. Preprocedural imaging of LI-RADS 5 hepatic tumors. A) Ultrasound image showing hepatocellular carcinoma (within arrows). The tumor demonstrated heterogenous echogenicity with predominant hyper-echogenicity and was multinodular with lobulated margins and pedunculated. Color Doppler ultrasound demonstrated large veins draining the tumor (asterisk). B) Coronal CT angiogram showing hypervascularity of the tumor (arrows) and large arteries supplying the tumor (asterisks) in an oblique multiplanar reconstruction displayed as maximum intensity projection of a 30-mm slab. The tumor arose from the left lateral lobe but was displaced to the right due to its size. (HA-hepatic artery; IVC-inferior vena cava; Ao-aorta). C) Coronal 0.4-mm-thick maximum intensity projection image acquired during the early arterial phase showing characteristic increased enhancement of the hepatocellular carcinoma (arrows) compared with liver without tumor (crosshatch). The artery supplying the tumor is shown (asterisk).
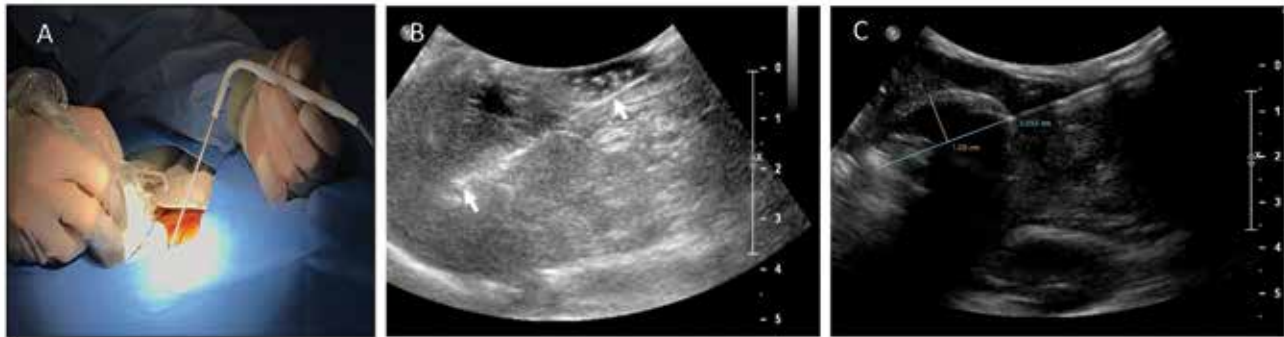
Figure 2. Cryoablation procedure. A) Cryoablation of LI-RADS 5 tumor with Ice Pearl 2.1 Cx 90° probe under ultrasound guidance. B) Placement of the probe (arrows) under ultrasound including the probe tip (left arrow). C) Ice ball formation during cryoablation with acoustic shadowing. Measurement of the long axis and the orthogonal short axis of the ice ball after the final freeze cycle are shown (OsiriX).

Table 1. Ice ball and cryolesion morphometrics

Imaging modality	Axial length (cm)	Short axis width (cm)	Cross section area (cm^2)	Volume (cm^3)
Ultrasound (n = 3), Day 0	3.1 ± 0.6	2.1 ± 0.1	4.7 ± 0.6[a,b]	
CT (n = 3), day 14	2.8 ± 0.3	2.6 ± 0.4, 2.9 ± 0.7	5.8 ± 1.3[a,c]	11.0 ± 3.8
Histology (n = 3)	2.7 ± 0.1	2.2 ± 0.4	4.7 ± 0.8[b,c]	

Ice ball and cryolesion morphometrics. There was no statistically detectable difference (paired t test) between cross sectional area measurements on ultrasound compared with CT,[a] ultrasound compared with histology,[b] and CT compared with histology.[c] Data from the first treated woodchuck (nonsurvival) are not included.

[a]$P > 0.59$
[b]$P > 0.96$
[c]$P > 0.17$

approximately 1 cm/10 s. The ice ball was visible during the initial freeze cycle and appeared elliptical. After the second freeze cycle, the ice ball had a clear echogenic rim with dense acoustic shadowing and appeared elliptical on US. The average ice ball dimensions were $3.1 \pm 0.6 \times 2.1 \pm 0.1$ cm with a calculated cross-sectional area of 4.7 ± 0.6 cm^2 (Table 1; Figures 2 and 3). Immediately after thawing and removal of the probe, the treated tissue was hypoechoic compared with untreated tumor tissue.

Cryolesion characterization on CT. CT acquired 14 d after ablation showed a devascularized hypo-attenuating cryolesion with an average volume of 11.0 ± 3.8 cm^3, maximum dimensions of $2.8 \pm 0.3 \times 2.6 \pm 0.4 \times 2.9 \pm 0.7$ cm and cross-sectional area of 5.8 ± 1.3 cm^2 (Table 1, Figure 3). The internal radiographic density of the ablation zone varied in degree of heterogeneity.

A 3D volumetric rendering of a target tumor and 14-d ablation zone CT showed an ellipsoidal shape cryoablation zone within the treated tumor, including the probe track cauterized during slow withdrawal of the cryoprobe (Figure 4).

Histopathology. The treated tumors were all confirmed as HCC by a board-certified veterinary pathologist. Hemorrhagic necrosis defined the treatment site of explanted tumors on gross inspection (Figure 3). The H and E stained cryolesion confirmed a region of coagulative necrosis bordered by a rim of karyorrhectic debris and a narrow rim of coagulative necrosis with an average width of 2.5 mm and fibrous connective tissue, clearly demarcating cryolesion from viable HCC. The internal appearance of the cyrolesions varied, each with unique areas of hemorrhage. The average cryolesion dimensions were
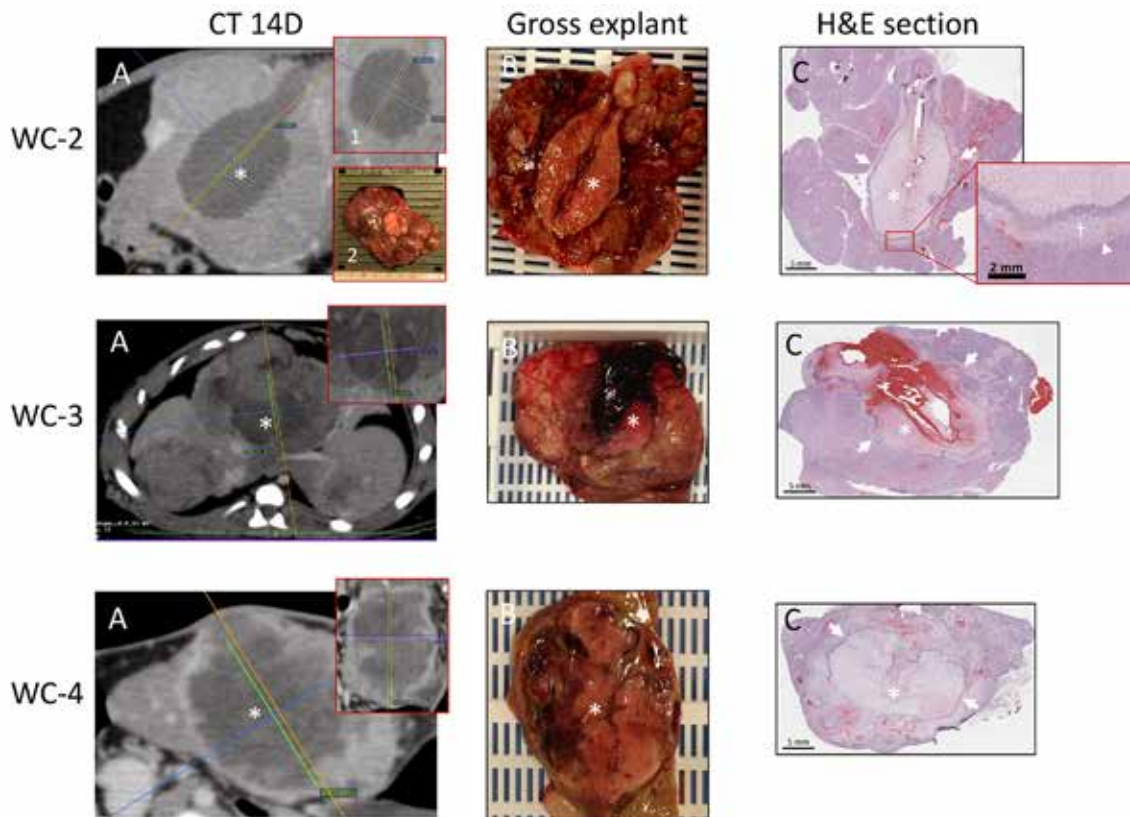
Figure 3. CT imaging and histopathology of cryoablation for each case. Column A) Multiphasic CT of the liver acquired during the portal phase 14 d after cryoablation. Multiplanar reconstruction was used to generate a plane that includes the probe track (orange line) and the orthogonal plane (inset 1). Devascularized hypo-attenuating cryolesions (asterisk) were present. Excised tumor tissue in the subject-specific mold (inset 2). Column B) Gross tumor pathology at explant showing cross-section (5-mm-thick slice) of the cryolesion zone (asterisk) and margins with hemorrhagic necrosis. Column C) Hematoxylin and eosin–stained cross-section of cryolesions showing probe tracks within a central amorphous region of coagulative necrosis (asterisks) bordered by a rim of karyorrhectic (leukocyte) debris (arrows). This was further surrounded by a narrow rim of coagulative necrosis with a mean width of 2.5 mm (WC-2 inset: dagger) encapsulated by a fibroblastic-rich collagenous connective tissue rim (arrowhead). The area outside the rim was defined as HCC with no cryo-related thermal injury.

$2.7 \pm 0.1 \times 2.2 \pm 0.4$ cm with a cross-sectional area of 4.7 ± 0.8 cm^2 (Table 1, Figure 3). In addition to the cryo-treated tumors, additional hepatic tumors of variable size and morphology were observed at gross pathology and confirmed to be HCC with occasional fibrosis and compression of surrounding parenchyma.

No statistically detectable difference (t test) was detected between cross sectional area measurements on US compared with CT ($P > 0.59$), US compared with histology ($P > 0.96$), and CT compared with histology ($P > 0.17$). A Pearson correlation analysis of cross-sectional area did not reveal correlation of US with CT ($P > 0.18$), US with histology ($P > 0.3$), or CT with histology ($P > 0.12$).

Discussion

This study demonstrated successful subtotal cryoablation of LI-RADS-5 tumors in woodchucks with hepatocellular carcinoma. The cross-sectional area of the ice ball and the ablation zone on CT and gross and histopathologic evaluation at 14 d were not statistically different from each other. The procedure was consistent and well-tolerated across all 3 animals. Although the cryoablation treatment algorithm was the same for all woodchucks, observed differences in cryolesion appearance may be due to tumor heterogeneity, including variable necrotic areas, vascularity, and areas of hemorrhage. We used subject-specific, 3D-printed cutting molds that were created based on segmented CT scans of the tumor at the time of ablation; these molds provided matching tissue sections for correlative imaging and gross and histopathologic evaluation as depicted in Figure 3A (inset 2) WC-2. At 14 days, the cryolesions had substantial coagulative necrosis based on CT and histology. However, we did not find a correlation between the cross-sectional area of the ice ball at US and the maximum dimension of the 14-d cryolesion on CT and histology evaluation, perhaps due to low statistical power.

We successfully performed subtotal cryoablation in 4 woodchucks, 3 of which recovered from anesthesia. The tumors in these woodchucks were similar to those of humans in absolute measured dimensions, permitting future hypothesis-driven inquiry regarding subtotal ablation without risk to adjacent structures that may be present in smaller animals. Furthermore, the multiplicity of tumors in a single woodchuck liver may permit study of abscopal effects.[20] Given the hypervascularity of the tumors, the cryoprobe track must be cauterized to prevent postablation hemorrhage. In the initial subject, the probe track was not cauterized upon probe withdrawal, resulting in hemodynamically significant hemorrhage that warranted euthanasia. In the remaining 3 woodchucks, the track was cauterized during probe withdrawal after the ablation, which prevented perceptible bleeding.

Percutaneous cryoablation is as effective as other ablation techniques (for example, radiofrequency and microwave ablation) for treating small HCC.[12] The growing use of immunotherapy combined with ablation to potentially augment the immunotherapy response has been implemented clinically, but has not yet been well characterized or widely adopted.[4,11,17]
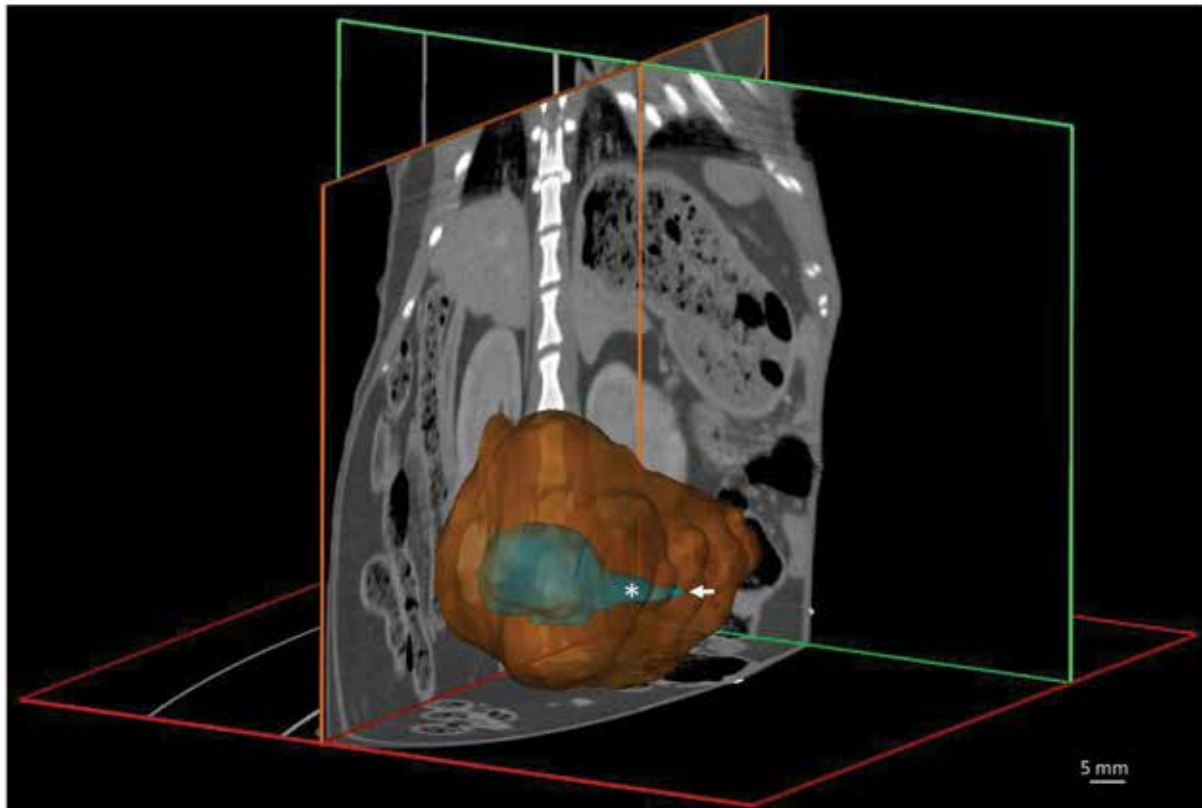
Figure 4. Multiplanar reconstruction of abdominal CT with 3D segmentation of the tumor and ablation zone. The elliptical cryoablation zone (blue) including the cryoprobe entry point (arrow) and cauterized cryoprobe track (asterisk) is shown within the pedunculated tumor (brown). This is the same ablation as shown in Figure 3, WC-2. The orthogonal axial (red), coronal (orange), and sagittal (green) imaging planes are shown.

The combination of cryoablation and immunostimulation has been shown to improve survival and suppress distant untreated tumor growth in a rabbit VX2 tumor model[16] and to promote a favorable antitumor response in mice as compared with radiofrequency or microwave alone.[31] However, a greater understanding of immune effects related to the use of ablation technology is needed to inform and optimize immunotherapy.[18,23] Given the biologic and imaging similarities of HCC in woodchucks to those of humans,[19,20] and with further immune characterization in the future, the study of woodchucks with HCC may facilitate the combination of ablative modalities with therapies designed to augment immunologic and abscopal responses associated with the treatment of HCC in humans.

The main limitation of this study was the small number of woodchucks used. Due to low sample size, our data were inadequate for addressing the correlational or predictive value of US or CT for final ablation size. Moreover, intraprocedural US images are subject to acoustic shadowing by the dense ice ball. The use of CT or MRI to monitor the tumor during ablation was not feasible in this study. CECTs were not conducted at completion of the cryoablation procedure, which precluded direct comparison of cryolesion size on CT at Day 0 and Day 14. Colocalization of CT with pathology was based on best cross-sectional matches of CT slices and pathology sections of spatially aligned tumor specimens using subject-specific 3D-printed cutting molds. However, tissue processing limitations and artifact may have been introduced during tissue sectioning. Future work may consider the value of intention-to-treat with complete ablation in woodchucks with less advanced disease, including development of a comprehensive assessment of the tumor response to treatment in woodchucks for comparison to humans. This line of study would include investigating the tumor and the cryolesion microenvironment, border characteristics, immune compartment analyses, flow cytometry, cross-species immune-correlation, immunohistochemistry, and treatment effect on non-HCC tissue.

In conclusion, image-guided cryoablation can be performed on woodchuck HCC with real-time visualization of the ice ball on US and delineation of the ablation zone on CECT. The cross sectional area of the ablation lesion and tissue necrosis on CT and histopathology at 14 d were comparable to the intraoperative ice ball on US. While additional characterization is needed, woodchuck HCC may provide a predictive preclinical model for investigation of ablative modalities and the development of new combination therapies including immunotherapeutics.

Disclaimer

The content of this manuscript does not necessarily reflect the views or policies of the U.S. Department of Health and Human Services. The mention of commercial products, their source, or their use in connection with material reported herein is not to be construed as an actual or implied endorsement of such products by the United States government.

References

1. **Buendia MA, Neuveut C.** 2015. Hepatocellular carcinoma. Cold Spring Harb Perspect Med **5**:a021444. https://doi.org/10.1101/cshperspect.a021444.

2. **Burke CT, Cullen JM, State A, Gadi S, Wilber K, Rosenthal M, Bulysheva A, Pease A, Mauro MA, Fuchs H.** 2011. Development of an animal model for radiofrequency ablation of primary, virally induced hepatocellular carcinoma in the woodchuck. J Vasc Interv Radiol **22**:1613–1618. https://doi.org/10.1016/j.jvir.2011.08.020.

3. **de Ruiter QMB, Xu S, Li M, Pritchard WF, Starost MF, Filie A, Mikhail AS, Mauda-Havakuk M, Esparza-Trujillo JA, Bakhutashvili I, Heidari P, Mahmood U, Karanian JW, Wood BJ.** 2021. Electromagnetic tracking and optical molecular imaging guidance for liver biopsy and point-of-care tissue assessment in phantom and woodchuck hepatocellular carcinoma. Cardiovasc Intervent Radiol **44**:1439–1447. https://doi.org/10.1007/s00270-021-02853-x.

4. **Duffy AG, Ulahannan SV, Makorova-Rusher O, Rahma O, Wedemeyer H, Pratt D, Davis JL, Hughes MS, Heller T, ElGindi M, Uppala A, Korangy F, Kleiner DE, Figg WD, Venzon D, Steinberg SM, Venkatesan AM, Krishnasamy V, Abi-Jaoudeh N, Levy E, Wood BJ, Greten TF.** 2017. Tremelimumab in combination with ablation in patients with advanced hepatocellular carcinoma. J Hepatol **66**:545–551. https://doi.org/10.1016/j.jhep.2016.10.029.

5. **Ei S, Hibi T, Tanabe M, Itano O, Shinoda M, Kitago M, Abe Y, Yagi H, Okabayashi K, Sugiyama D, Wakabayashi G, Kitagawa Y.** 2015. Cryoablation provides superior local control of primary hepatocellular carcinomas of >2 cm compared with radiofrequency ablation and microwave coagulation therapy: An underestimated tool in the toolbox. Ann Surg Oncol **22**:1294–1300. https://doi.org/10.1245/s10434-014-4114-7.

6. **Erinjeri JP, Clark TW.** 2010. Cryoablation: Mechanism of action and devices. J Vasc Interv Radiol **21**:S187–S191. https://doi.org/10.1016/j.jvir.2009.12.403.

7. **Etheridge ML, Choi J, Ramadhyani S, Bischof JC.** 2013. Methods for characterizing convective cryoprobe heat transfer in ultrasound gel phantoms. J Biomech Eng **135**:021002. https://doi.org/10.1115/1.4023237.

8. **Fairman J, Liu KH, Menne S.** 2017. Prevention of liver tumor formation in woodchucks with established hepatocellular carcinoma by treatment with cationic liposome-DNA complexes. BMC Cancer **17**:172. https://doi.org/10.1186/s12885-017-3163-2.

9. **Gaba R, Obeid M, Khabbaz R, Garcia K, Schachtschneider K.** 2018. Translational animal models for liver cancer. American Journal of Interventional Radiology **2**:1–8. https://doi.org/10.25259/AJIR-11-2017.

10. **Global Burden of Disease Cancer Collaboration,** Fitzmaurice C, Allen C, Barber RM, Barregard L, Bhutta ZA, Brenner H, Dicker DJ, Chimed-Orchir O, Dandona R, Dandona L, Fleming T, Forouzanfar MH, Hancock J, Hay RJ, Hunter-Merrill R, Huynh C, Hosgood HD, Johnson CO, Jonas JB, Khubchandani J, Kumar GA, Kutz M, Lan Q, Larson HJ, Liang X, Lim SS, Lopez AD, MacIntyre MF, Marczak L, Marquez N, Mokdad AH, Pinho C, Pourmalek F, Salomon JA, Sanabria JR, Sandar L, Sartorius B, Schwartz SM, Shackelford KA, Shibuya K, Stanaway J, Steiner C, Sun J, Takahashi K, Vollset SE, Vos T, Wagner JA, Wang H, Westerman R, Zeeb H, Zoeckler L, Abd-Allah F, Ahmed MB, Alabed S, Alam NK, Aldhahri SF, Alem G, Alemayohu MA, Ali R, Al-Raddadi R, Amare A, Amoako Y, Artaman A, Asayesh H, Atnafu N, Awasthi A, Saleem HB, Barac A, Bedi N, Bensenor I, Berhane A, Bernabe E, Betsu B, Binagwaho A, Boneya D, Campos-Nonato I, Castaneda-Orjuela C, Catala-Lopez F, Chiang P, Chibueze C, Chitheer A, Choi JY, Cowie B, Damtew S, das Neves J, Dey S, Dharmaratne S, Dhillon P, Ding E, Driscoll T, Ekwueme D, Endries AY, Farvid M, Farzadfar F, Fernandes J, Fischer F, TT GH, Gebru A, Gopalani S, Hailu A, Horino M, Horita N, Husseini A, Huybrechts I, Inoue M, Islami F, Jakovljevic M, James S, Javanbakht M, Jee SH, Kasaeian A, Kedir MS, Khader YS, Khang YH, Kim D, Leigh J, Linn S, Lunevicius R, El Razek HMA, Malekzadeh R, Malta DC, Marcenes W, Markos D, Melaku YA, Meles KG, Mendoza W, Mengiste DT, Meretoja TJ, Miller TR, Mohammad KA, Mohammadi A, Mohammed S, Moradi-Lakeh M, Nagel G, Nand D, Le Nguyen Q, Nolte S, Ogbo FA, Oladimeji KE, Oren E, Pa M, Park EK, Pereira DM, Plass D, Qorbani M, Radfar A, Rafay A, Rahman M, Rana SM, Soreide K, Satpathy M, Sawhney M, Sepanlou SG, Shaikh MA, She J, Shiue I, Shore HR, Shrime MG, So S, Soneji S, Stathopoulou V, Stroumpoulis K, Sufiyan MB, Sykes BL, Tabares-Seisdedos R, Tadese F, Tedla BA, Tessema GA, Thakur JS, Tran BX, Ukwaja KN, Uzochukwu BSC, Vlassov VV, Weiderpass E, Wubshet Terefe M, Yebyo HG, Yimam HH, Yonemoto N, Younis MZ, Yu C, Zaidi Z, Zaki MES, Zenebe ZM, Murray CJL, Naghavi M.** 2017. Global, regional, and national cancer incidence, mortality, years of life lost, years lived with disability, and disability-adjusted life-years for 32 cancer groups, 1990 to 2015: A systematic analysis for the global burden of disease study. JAMA Oncol **3**:524–548. https://doi.org/10.1001/jamaoncol.2016.5688.

11. **Greten TF, Mauda-Havakuk M, Heinrich B, Korangy F, Wood BJ.** 2019. Combined locoregional-immunotherapy for liver cancer. J Hepatol **70**:999–1007. https://doi.org/10.1016/j.jhep.2019.01.027.

12. **Gupta P, Maralakunte M, Kumar MP, Chandel K, Chaluvashetty SB, Bhujade H, Kalra N, Sandhu MS.** 2021. Overall survival and local recurrence following RFA, MWA, and cryoablation of very early and early HCC: A systematic review and Bayesian network meta-analysis. Eur Radiol **31**:5400–5408. https://doi.org/10.1007/s00330-020-07610-1.

13. **Hafid M, Lacroix M.** 2017. Fast inverse prediction of the freezing front in cryosurgery. J Therm Biol **69**:13–22. https://doi.org/10.1016/j.jtherbio.2017.05.008.

14. **Huang KW, Wu HL, Lin HL, Liang PC, Chen PJ, Chen SH, Lee HI, Su PY, Wu WH, Lee PH, Hwang LH, Chen DS.** 2010. Combining antiangiogenic therapy with immunotherapy exerts better therapeutical effects on large tumors in a woodchuck hepatoma model. Proc Natl Acad Sci USA **107**:14769–14774. https://doi.org/10.1073/pnas.1009534107.

15. **Jacob JR, Sterczer A, Toshkov IA, Yeager AE, Korba BE, Cote PJ, Buendia MA, Gerin JL, Tennant BC.** 2004. Integration of woodchuck hepatitis and N-myc rearrangement determine size and histologic grade of hepatic tumors. Hepatology **39**:1008–1016. https://doi.org/10.1002/hep.20106.

16. **Kageyama K, Yamamoto A, Okuma T, Hamamoto S, Takeshita T, Sakai Y, Nishida N, Matsuoka T, Miki Y.** 2013. Radiofrequency ablation of liver tumors in combination with local OK-432 injection prolongs survival and suppresses distant tumor growth in the rabbit model with intra- and extrahepatic VX2 tumors. Cardiovasc Intervent Radiol **36**:1383–1392. https://doi.org/10.1007/s00270-013-0650-y.

17. **Lawal G, Xiao Y, Rahnemai-Azar AA, Tsilimigras DI, Kuang M, Bakopoulos A, Pawlik TM.** 2021. The Immunology of Hepatocellular Carcinoma. Vaccines (Basel) **9**:1184.

18. **Liu P, Jia S, Lou Y, He K, Xu LX.** 2019. Cryo-thermal therapy inducing MI macrophage polarization created CXCL10 and IL-6-rich pro-inflammatory environment for CD4(+) T cell-mediated anti-tumor immunity. Int J Hyperthermia **36**:408–420. https://doi.org/10.1080/02656736.2019.1579373.

19. **Mauda-Havakuk M, Kassin MT, Mikhail AS, Esparza-Trujillo JA, Bakhutashvili I, Woods DL, Wakim PG, Starost MF, Karanian JW, Wood BJ, Pritchard WF.** 2022. Woodchuck hepatic anatomy and vascular alterations due to hepatocellular carcinoma with angiographic atlas of the abdomen and pelvis.

J Vasc Interv Radiol **33**:316–323. https://doi.org/10.1016/j.jvir.2021.11.005.

20. **Mauda-Havakuk M, Mikhail AS, Starost MF, Jones EC, Karim B, Kleiner DE, Partanen A, Esparza-Trujillo JA, Bakhutashvili I, Wakim PG, Kassin MT, Lewis AL, Karanian JW, Wood BJ, Pritchard WF.** 2021. Imaging, pathology, and immune correlates in the woodchuck hepatic tumor model. J Hepatocell Carcinoma **8**:71–83. https://doi.org/10.2147/JHC.S287800.

21. **Mikhail AS, Mauda-Havakuk M, Partanen A, Karanian JW, Pritchard WF, Wood BJ.** 2020. Liver-specific 3D sectioning molds for correlating in vivo CT and MRI with tumor histopathology in woodchucks (*Marmota monax*). PLoS One **15**:e0230794. https://doi.org/10.1371/journal.pone.0230794.

22. **Nachabé R, Hendriks BHW, Schierling R, Hales J, Racadio JM, Rottenberg S, Ruers TJM, Babic D, Racadio JM.** 2015. Real-time in vivo characterization of primary liver tumors with diffuse optical spectroscopy during percutaneous needle interventions: Feasibility study in woodchucks. Invest Radiol **50**:443–448. https://doi.org/10.1097/RLI.0000000000000149.

23. **Pahk KJ, Shin CH, Bae IY, Yang Y, Kim SH, Pahk K, Kim H, Oh SJ.** 2019. Boiling histotripsy-induced partial mechanical ablation modulates tumour microenvironment by promoting immunogenic cell death of cancers. Sci Rep **9**:9050. https://doi.org/10.1038/s41598-019-45542-z.

24. **Popper H, Roth L, Purcell RH, Tennant BC, Gerin JL.** 1987. Hepatocarcinogenicity of the woodchuck hepatitis virus. Proc Natl Acad Sci USA **84**:866–870. https://doi.org/10.1073/pnas.84.3.866.

25. **Pritchard WF, Woods DL, Esparza-Trujillo JA, Starost MF, Mauda-Havakuk M, Mikhail AS, Bakhutashvili I, Leonard S, Jones EC, Krishnasamy V, Karanian JW, Wood BJ.** 2020. Transarterial chemoembolization in a woodchuck model of hepatocellular carcinoma. J Vasc Interv Radiol **31**:812–819. https://doi.org/10.1016/j.jvir.2019.08.031.

26. **Ratanaprasatporn L, Sainani N, Duda JB, Aghayev A, Tatli S, Silverman SG, Shyn PB.** 2019. Imaging findings during and after percutaneous cryoablation of hepatic tumors. Abdom Radiol (NY) **44**:2602–2626. https://doi.org/10.1007/s00261-019-01999-0.

27. **Rong G, Bai W, Dong Z, Wang C, Lu Y, Zeng Z, Qu J, Lou M, Wang H, Gao X, Chang X, An L, Li H, Chen Y, Hu KQ, Yang Y.** 2015. Long-term outcomes of percutaneous cryoablation for patients with hepatocellular carcinoma within Milan criteria. PLoS One **10**:e0123065. https://doi.org/10.1371/journal.pone.0123065.

28. **Song KD.** 2016. Percutaneous cryoablation for hepatocellular carcinoma. Clin Mol Hepatol **22**:509–515. https://doi.org/10.3350/cmh.2016.0079.

29. **Tennant BC, Toshkov IA, Peek SF, Jacob JR, Menne S, Hornbuckle WE, Schinazi RD, Korba BE, Cote PJ, Gerin JL.** 2004. Hepatocellular carcinoma in the woodchuck model of hepatitis B virus infection. Gastroenterology **127**:S283–S293. https://doi.org/10.1053/j.gastro.2004.09.043.

30. **Wilkins LR, Stone JR, Mata J, Hawrylack A, Kubicka E, Brautigan DL.** 2017. The use of the woodchuck as an animal model for evaluation of transarterial embolization. J Vasc Interv Radiol **28**:1467–1471. https://doi.org/10.1016/j.jvir.2017.04.005.

31. **Yakkala C, Chiang CL, Kandalaft L, Denys A, Duran R.** 2019. Cryoablation and immunotherapy: An enthralling synergy to confront the tumors. Front Immunol **10**:2283. https://doi.org/10.3389/fimmu.2019.02283.